Journal of Molecular Spectroscopy 264 (2010) 83–93

Contents lists available at ScienceDirect

Journal of Molecular Spectroscopy

journal homepage: www.elsevier.com/locate/jms

Rovibrational structure and potential energy function of the $X\,0^+$ ground electronic state of ArXe

Lorena Piticco [a], Frédéric Merkt [a,*], Aleksander A. Cholewinski [b], Frederick R.W. McCourt [b], Robert J. Le Roy [b]

[a] Laboratorium für Physikalische Chemie, ETH Zürich, CH 8093 Zürich, Switzerland
[b] Department of Chemistry, University of Waterloo, Waterloo, ON, N2L 3G1 Canada

ARTICLE INFO

Article history:
Received 3 March 2010
In revised form 30 July 2010
Available online 18 October 2010

Keywords:
ArXe
ArXe spectroscopy
ArXe potential energy function
VUV laser spectroscopy

ABSTRACT

Rotationally resolved $(1+1')$ resonance-enhanced two-photon ionization spectra of the $D\,0^+, C\,1 \leftarrow X\,0^+$ band systems of several isotopomers of ArXe were recorded at high resolution in the wave-number range from 77000 cm^{-1} to 77300 cm^{-1} using a near-Fourier-transform-limited vacuum-ultraviolet laser system. The rotational structure of the $v''=0,1$ vibrational levels of the $X\,0^+$ ground state of ArXe could be fully resolved and assigned, leading to a new set of spectroscopic parameters. A 'direct potential fit' to a combination of these data with microwave spectroscopy results [W. Jäger et al., J. Chem. Phys. 99 (1993) 919–927] and virial coefficients yields an accurate new potential energy function with equilibrium distance $R_e = 4.095773(29)$ Å and well depth $\mathfrak{D}_e = 129.81(38)$ cm^{-1}.

1. Introduction

Spectroscopic investigation of the ground and excited electronic states of the rare-gas dimers and their singly-charged ions is of fundamental interest, as it provides important information on the structural and dynamical properties of these species. Electronic transitions from a bound excited state to a lower-lying repulsive state in *excimer* (*excited dimer*) molecules can be used as vacuum ultraviolet radiation sources [1,2].

In their electronic ground state, rare-gas dimers have potential energy functions that are repulsive at short internuclear distances and have a shallow well at large distances, and they are ideal model systems for studying van der Waals interactions (see, for instance [3–6]). High-quality potential energy functions of the electronic ground state of homonuclear and heteronuclear rare-gas dimers have been derived by semiempirical methods [7–9]. Potential energy functions that provide quite good predictions of spectroscopic properties have also been determined by ab initio quantum chemical methods for the lighter dimers [10–12]. However, as the number of electrons increases, the ab initio computations become more demanding, and the semi-empirical analysis of experimental data remains the best way of determining accurate potential energy functions for the heavier rare-gas pairs.

Spectroscopic data from which information on the ground electronic state of the heavier heteronuclear dimers can be derived are still very scarce. In the case of ArXe, it is limited to high-resolution measurements of pure rotational transitions in the $X\,0^+$ $v''=0$ ground state for seven isotopomers [13], and lower resolution studies of several electronic band systems in the vacuum ultraviolet [14–18]. The three leading rotational constants for the ground vibronic state of the six main isotopomers [e.g., $B_0 = 961.29377(4)$ MHz, $D_0 = 6.64655(78)$ MHz and $H_0 = -0.1714(51)$ MHz for $^{40}Ar^{132}Xe$] were obtained from microwave spectra by Jäger et al. [13], who used their results for different isotopomers to predict a ground $X\,0^+$ state equilibrium internuclear separation of $R_e = 4.094(5)$ Å. Liu and coworkers [17] recorded spectra of the C 1, D $0^+ \leftarrow X\,0^+$ transitions at a resolution of 0.09 cm^{-1}, sufficient to partially resolve the rotational structure. However, their analysis focused on the rotational structure of the excited states and not on the $X\,0^+$ state, for which they adopted the rotational constants from the microwave spectroscopic study. Thus, prior to the present work there existed no direct observation of the vibrational structure of the ground $X\,0^+$ state of ArXe.

We describe here measurements of fully rotationally resolved spectra of the C 1, D $0^+ \leftarrow X\,0^+$ electronic transitions of selected isotopomers of ArXe, from which we have determined the low energy rovibrational level structure of the $X\,0^+$ ground state. This information was then combined with the microwave data to determine sets of conventional spectroscopic constants for $Ar^{132}Xe$ and $Ar^{136}Xe$. These spectroscopic data were then combined with interaction virial coefficients for this system [19–21] in a direct-potential-fit data analysis which yielded an accurate analytic potential energy function for the $X\,0^+$ ground state of ArXe.

2. Experiment

The spectra of the C 1, D $0^+ \leftarrow X\,0^+$ transitions of ArXe have been recorded using the narrow-bandwidth (full width at half

* Corresponding author.
E-mail address: feme@xuv.phys.chem.ethz.ch (F. Merkt).

0022-2852/$ - see front matter © 2010 Elsevier Inc. All rights reserved.
doi:10.1016/j.jms.2010.08.007

maximum of 0.008 cm^{-1}) VUV laser system coupled to a time-of-flight mass spectrometer described in Ref. [22]. Only technical features relevant to the present investigation are summarized here. The tunable vacuum-ultraviolet radiation (VUV, $\tilde{\nu}_{VUV} = 2\tilde{\nu}_{UV} - \tilde{\nu}_2$) was produced by two-photon resonance-enhanced difference-frequency mixing in a Kr cell using the $4p^5(^2P_{3/2})5p[1/2](J = 0) \leftarrow 4p^6\ ^1S_0$ two-photon transition of Kr at $2\tilde{\nu}_{UV} = 94092.906\ cm^{-1}$. The four-wave mixing process was resonantly enhanced by locking the wave number $\tilde{\nu}_{UV} = 3\tilde{\nu}_1$ of the tripled output of the first pulsed dye laser to the two-photon resonance. The locking was achieved by stabilizing the fundamental frequency of the dye laser to a hyperfine component in the saturated absorption spectrum of molecular iodine [23].

The VUV wave number was tuned by scanning the wave number $\tilde{\nu}_2$ of the second pulsed dye laser which was calibrated by recording several étalon spectra and a laser-induced-fluorescence spectrum of I_2 with each spectrum. The absolute VUV wave numbers could be calibrated with an accuracy of 0.02 cm^{-1}, and thanks to the étalon spectra, relative spectral positions could be determined with a precision of better than 0.002 cm^{-1}.

Two beams with wave numbers $\tilde{\nu}_1$ and $\tilde{\nu}_2$ were generated from single-mode cw ring dye lasers which were pulse amplified in three dye cells pumped by the second harmonic of a Nd:YAG laser and frequency doubled (tripled) in β-barium-borate crystals. The resulting difference-frequency beam was separated from the beams of wave numbers $\tilde{\nu}_{UV}$ and $\tilde{\nu}_2$ using a LiF prism, and directed into the excitation region where the VUV laser beam crossed a skimmed, pulsed supersonic beam obtained by expanding into vacuum a 10:1 mixture of Ar and Xe held at a nozzle stagnation pressure of 1.5 bar. The nozzle operating conditions were optimized so as to maximize the concentration of ArXe and to avoid the formation of too high densities of Ar_nXe_m clusters with $n, m > 1$.

The spectra of the $C \leftarrow X$ and $D \leftarrow X$ transitions were recorded by monitoring the ions produced by $(1 + 1')$ resonance-enhanced two-photon ionization as a function of the wave number of the VUV laser. The ionization from the states excited by the VUV laser was induced by the third harmonic (wavelength of 355 nm) of the same Nd:YAG laser that was used to pump the amplification stages. The ions were extracted by applying pulsed voltages to a set of cylindrical extraction plates and detected mass selectively at the end of a time-of-flight (TOF) tube using a microchannel-plate (MCP) detector. The ion signals were displayed on a digital oscilloscope, averaged over a preset number of laser pulses, and transferred to a computer.

The mass resolution of the TOF spectra was sufficient to cleanly separate the ion signals of the different isotopomers. By setting adequate temporal gates in the TOF mass spectra and monitoring the ion signals in these gates as a function of the VUV wave number, spectra of the six dominant isotopomers of ArXe ($^{40}Ar^{129}Xe$ (natural abundance 26.3%), $^{40}Ar^{130}Xe$ (4.1%), $^{40}Ar^{131}Xe$ (21.1%), $^{40}Ar^{132}Xe$ (26.8%), $^{40}Ar^{134}Xe$ (10.4%), $^{40}Ar^{136}Xe$ (8.8%) [24]) were recorded simultaneously.

3. Experimental results

The $(1 + 1')$ two-photon ionization spectrum of ArXe in the region of the $D\ 0^+ \leftarrow X\ 0^+$ transition is depicted in Fig. 1. This spectrum, taken from Ref. [18], was recorded at a resolution of 0.6 cm^{-1}, and consists primarily of transitions from the $v'' = 0$ level of the $X\ 0^+$ ground state to the $v' = 0 - 3$ levels of the $D\ 0^+$ and the $v' = 5 - 7$ levels of the C 1 state. In the course of the present study, several extremely weak lines of this spectrum could be assigned to hot bands, such as the $D\ 0^+(v' = 0 - 2) \leftarrow X\ 0^+(v'' = 1)$ and the C 1 $(v' = 7) \leftarrow X\ 0^+(v'' = 1)$ bands, on the basis of their rotational structures (see below).

High-resolution spectra of all bands indicated along the assignment bars in Fig. 1 have been recorded at a resolution of 0.01 cm^{-1}, which is sufficient to resolve the rotational structure. The hot bands are of particular significance for the study of the $X\ 0^+$ ground state of ArXe, because their analysis permits the extraction of information not available from earlier studies. Perturbations in the structure of the C state [25,26] made the $C \leftarrow X$ transitions unsuitable for the analysis of the rovibrational structure of the $X\ 0^+$ ground state, and for this reason we chose to use only the $D\ 0^+(v' = 0 - 3) \leftarrow X\ 0^+(v'' = 0, 1)$ transitions. In order to observe spectra of the very weak hot bands seen in Fig. 1 with satisfactory signal-to-noise ratio, it was necessary to increase the temperature of the supersonic expansion. This was achieved by modifying the operating conditions of the nozzle, primarily the nozzle opening time with respect to the laser pulse.

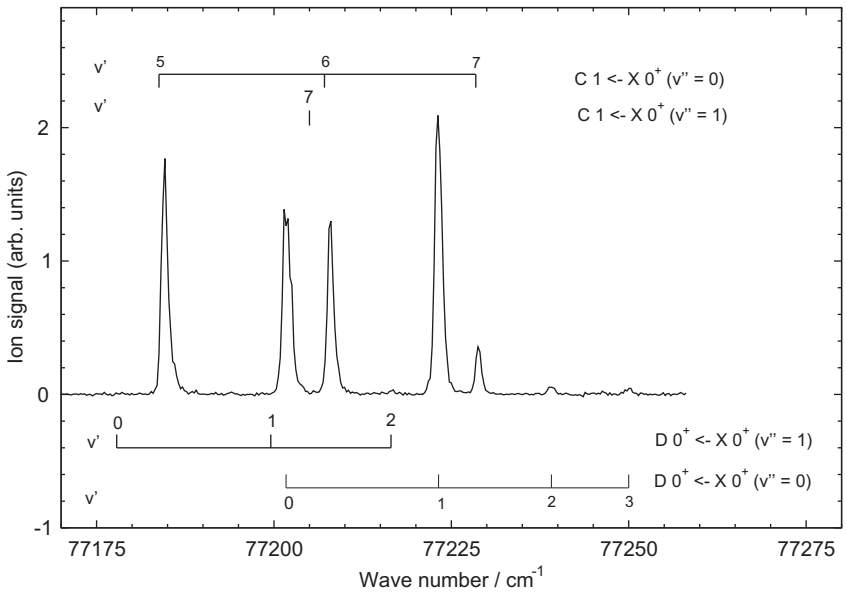

Fig. 1. Resonance-enhanced $1_{VUV} + 1'$ two-photon ionization spectra of the transitions from the $X\ 0^+$ ground state of $^{40}Ar^{129}Xe$ to the $D\ 0^+$ and C 1 Rydberg states in the vicinity of the $Xe^*([5p]^5 6s'[1/2]_1) + Ar(^1S_0)$ dissociation limit (adapted from reference [18]).

As illustrations of the information content of the high-resolution spectra, Figs. 2 and 3 show, as inverted traces, high-resolution spectra of the D $0^+(v'=2) \leftarrow$ X $0^+(v''=0,1)$ transitions of the $^{40}Ar^{132}Xe$ and $^{40}Ar^{136}Xe$ isotopomers, respectively. These spectra show the P- and R-branch structure characteristic of a $0^+ \leftarrow 0^+$ electronic transition, and the spectral assignments, indicated above the spectra, are straightforward. In each figure, the upper panel (a) corresponds to the transition from the $v''=0$ ground state and the lower panel (b) to the transition from the $v''=1$ level. The signal-to-noise ratio is poorer for the weaker hot bands and for the less abundant isotopomer.

The warmer temperature of the sample used to record the hot bands is immediately recognizable from the much larger number of lines in each branch. From the analysis of the intensity distributions, a rotational temperature of 3.5 K was obtained for the spectra of the transition from the $v''=0$ level (Figs. 2a and 3a), and of 8.5 K for the hot bands (Figs. 2b and 3b). At the higher temperature used to record the hot bands, rotational levels of the $v''=0$ ground

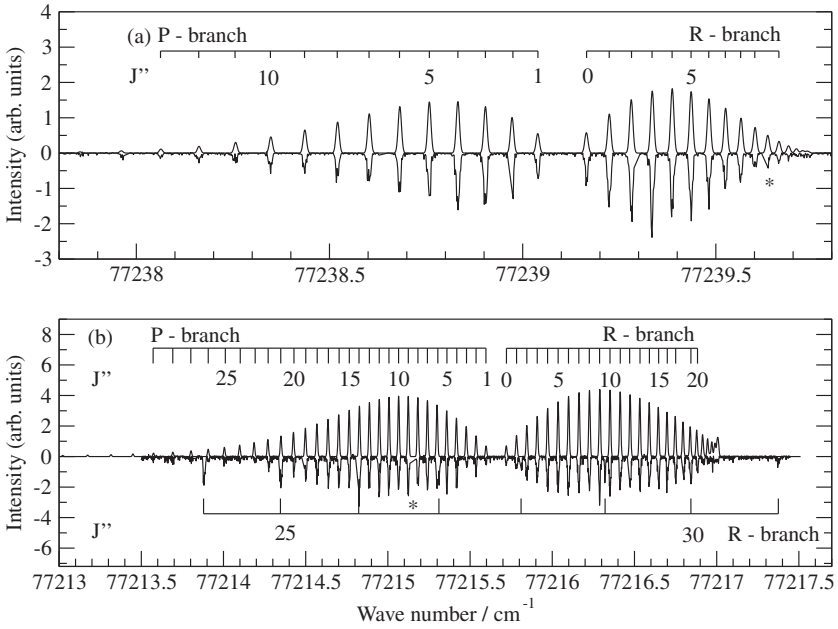

Fig. 2. Rotationally resolved spectra of the D $0^+(v'=2) \leftarrow$ X $0^+(v''=0)$ (upper panel) and D $0^+(v'=2) \leftarrow$ X $0^+(v''=1)$ (lower panel) transitions of $^{40}Ar^{132}Xe$. In each panel, the experimental spectra are shown as lower, inverted traces, and spectra calculated with the spectroscopic constants determined by a least-squares fit as upper traces. The rotational structure shown in the upper (lower) panel was calculated assuming a rotational temperature of 3.5 K (8.5 K). The assignment bars indicate the positions of the R(J'') and P(J'') transitions. High-J lines of the R branch of the C $1(v'=6) \leftarrow$ X $0^+(v''=0)$ are also observed in the spectrum of the hot band. In the regions marked by asterisks, mode hops of the ring laser made the spectra unusable.

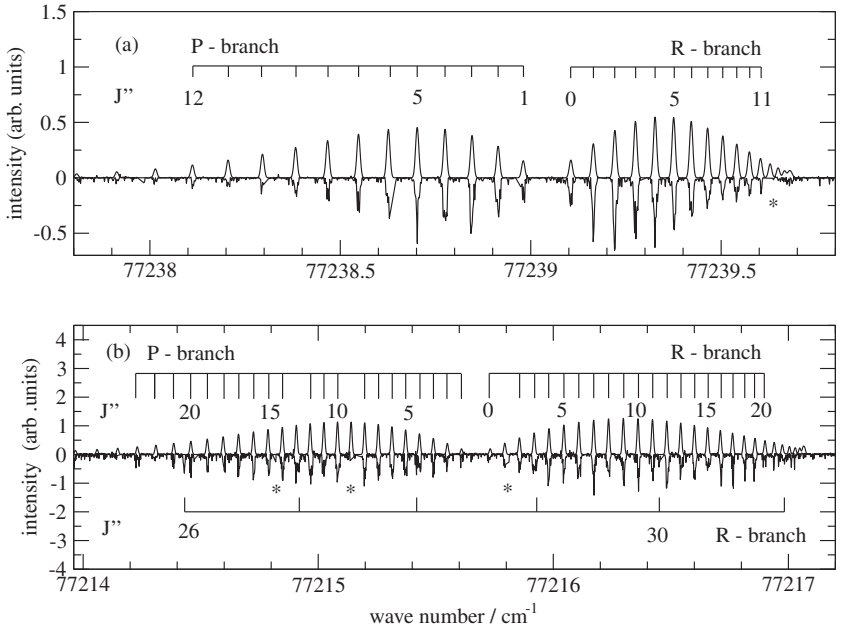

Fig. 3. As in Fig. 2 for the D $0^+(v'=2) \leftarrow$ X $0^+(v''=0)$ (upper panel) and D $0^+(v'=2) \leftarrow$ X $0^+(v''=1)$ (lower panel) transitions of $^{40}Ar^{136}Xe$.

state with J'' as high as 31 are populated, and the rotational structure of the D 0^+ $v' = 2 \leftarrow$ X 0^+ $v'' = 1$ band overlaps with the high-J end of the R-branch of the C $1 \leftarrow X\ 0^+$ $v'' = 0$ band, as indicated by the assignment bars placed below the spectra in Figs. 2b and 3b.

The observed transitions are presented in Tables 1 and 2, and the positions of all observed rovibrational levels of the X 0^+ ground state of ArXe, determined from combination differences, are summarized in the third column of Table 3 where they are compared with predictions generated from fitted analytic potential energy functions with two (fourth column) and four (fifth column) adjustable parameters, as explained in Section 4. The transition wave numbers could also be analyzed using standard expressions for a $0^+ \leftrightarrow 0^+$ transition:

$$\tilde{\nu} = \tilde{\nu}_{v'v''} + F_{v'}(J') - F_{v''}(J'') \quad (1)$$

with

$$F_v(J) = B_v J(J+1) - D_v J^2(J+1)^2 + H_v J^3(J+1)^3. \quad (2)$$

Band constants were therefore determined from a combined fit of our observed VUV line positions and the rotational transitions reported in Ref. [13] to Eqs. (1) and (2). Because of the higher resolution of the microwave spectra, the weights of the pure rotational transitions were chosen to be typically a factor of 10^8 larger than the weights of the VUV transitions. The resulting empirical molecular constants are listed in Table 4, where they are compared with previous results. These fitted parameters are in excellent agreement with those obtained in Ref. [13], and the ground state rovibrational energies differ slightly from those implied by the empirical potential function of Aziz and van Dalen [3]. However, because of the limited range of J, these centrifugal distortion constants differ somewhat from the 'mechanically consistent' values implied by the best fitted potential energy function, especially for $v'' = 1$.

4. Determination of the ground state potential curve of ArXe

4.1. The 'direct-potential-fit' procedure

Previous efforts to determine the potential energy function of the $X\ 0^+$ state of ArXe have relied either on the application of

Table 1
Measured wave numbers (in cm^{-1}) and differences with calculated results ($\Delta\tilde{\nu} = \tilde{\nu}_{exp} - \tilde{\nu}_{calc}$ in cm^{-1}) obtained from the band constants of Table 5 ($\Delta\tilde{\nu}$(bc)) or generated using the MLR potential of Table 7 ($\Delta\tilde{\nu}$(MLR)), for transitions from the $v'' = 0, 1$ vibrational levels of the X 0^+ ground state of $^{40}Ar^{132}Xe$ to the $v' = 2$ vibrational level of the excited D 0^+ state. The uncertainties correspond to the relative experimental standard deviations (the uncertainty in the absolute wave numbers is 0.015).

	$v'' = 0 \rightarrow v' = 2$			$v'' = 1 \rightarrow v' = 2$		
	$\tilde{\nu}_{exp}$	$\Delta\tilde{\nu}$(bc)	$\Delta\tilde{\nu}$(MLR)	$\tilde{\nu}_{exp}$	$\Delta\tilde{\nu}$(bc)	$\Delta\tilde{\nu}$(MLR)
R(0)	77239.1655(12)	0.0008	−0.0003	77215.7212(11)	0.0012	0.0004
R(1)	77239.2240(12)	−0.0002	−0.0009	77215.7830(11)	0.0007	0.0001
R(2)	77239.2817(10)	0.0007	−0.0003	77215.8451(11)	0.0001	−0.0008
R(3)	77239.3348(11)	−0.0005	−0.0010	77215.9086(11)	0.0004	0.0001
R(4)	77239.3867(08)	−0.0004	0.0000	77215.9716(11)	−0.0001	0.0003
R(5)	77239.4358(11)	−0.0003	−0.0001	77216.0355(11)	0.0001	0.0003
R(6)	77239.4817(10)	−0.0005	0.0000	77216.0986(11)	−0.0005	−0.0004
R(7)	77239.5245(11)	−0.0007	0.0002	77216.1615(11)	−0.0014	−0.0008
R(8)	77239.5641(11)	−0.0011	0.0002	77216.2254(11)	−0.0010	−0.0003
R(9)	77239.6008(14)	−0.0008	0.0008	77216.2879(11)	−0.0015	−0.0006
R(10)				77216.3511(11)	−0.0008	−0.0003
R(11)	77239.6631(11)	−0.0003	0.0008	77216.4135(11)	0.0001	0.0001
R(12)				77216.4707(11)	−0.0032	−0.0015
R(13)				77216.5334(11)	0.0004	0.0002
R(14)				77216.5910(11)	0.0005	−0.0004
R(15)				77216.6471(11)	0.0012	−0.0004
R(16)				77216.6993(11)	0.0002	−0.0001
R(17)				77216.7507(11)	0.0011	0.0000
R(20)				77216.8833(48)	0.0018	−0.0002
P(1)	77239.0395(11)	0.0006	0.0005	77215.5964(11)	−0.0007	−0.0006
P(2)	77238.9747(14)	0.0023	0.0013	77215.5363(11)	−0.0002	−0.0010
P(3)	77238.9035(11)	0.0000	0.0007	77215.4784(11)	0.0021	0.0014
P(4)	77238.8323(15)	−0.0002	0.0009	77215.4193(11)	0.0026	0.0015
P(5)	77238.7585(15)	−0.0002	0.0002	77215.3591(11)	0.0014	0.0009
P(6)	77238.6811(12)	−0.0008	0.0004			
P(7)	77238.6023(14)	−0.0006	0.0003	77215.2406(11)	0.0001	0.0000
P(8)	77238.5201(11)	−0.0009	0.0004	77215.1829(11)	0.0007	0.0006
P(9)	77238.4354(11)	−0.0008	0.0002	77215.1240(11)	0.0001	0.0003
P(10)	77238.3471(16)	−0.0011	0.0001	77215.0652(11)	−0.0004	0.0001
P(11)	77238.2554(14)	−0.0015	0.0001	77215.0063(11)	−0.0007	−0.0001
P(12)	77238.1615(20)	−0.0007	0.0007	77214.9476(11)	−0.0003	−0.0001
P(13)	77238.0626(14)	−0.0010	0.0000	77214.8873(11)	−0.0008	−0.0010
P(14)	77237.9631(20)	0.0020	0.0049			
P(15)				77214.7656(11)	0.0001	−0.0003
P(16)				77214.7035(11)	0.0015	0.0003
P(17)	77237.6269(10)	0.0004	0.0004	77214.6384(16)	0.0015	−0.0002
P(18)				77214.5701(11)	0.0005	0.0001
P(19)				77214.5007(22)	0.0007	−0.0005
P(20)				77214.4289(11)	0.0013	0.0000
P(22)				77214.2750(25)	0.0022	0.0000
P(23)				77214.1913(38)	0.0016	0.0001
P(24)				77214.0992(75)	−0.0030	0.0001
P(26)				77213.9081(34)	−0.0041	0.0000
P(28)				77213.6942(60)	−0.0046	0.0001
P(29)				77213.5717(50)	−0.0103	0.0000

Table 2
As in Table 1, for $^{40}Ar^{136}Xe$.

	$v'' = 0 \rightarrow v' = 2$			$v'' = 1 \rightarrow v' = 2$		
	$\tilde{\nu}_{exp}$	$\Delta\tilde{\nu}$(bc)	$\Delta\tilde{\nu}$(MLR)	$\tilde{\nu}_{exp}$	$\Delta\tilde{\nu}$(bc)	$\Delta\tilde{\nu}$(MLR)
R(0)	77239.1048(11)	−0.0008	0.0000	77215.7276(34)	−0.0030	−0.0026
R(1)	77239.1646(11)	0.0001	0.0001			
R(2)	77239.2206(11)	−0.0006	−0.0006	77215.8570(16)	0.0021	0.0016
R(3)	77239.2755(13)	0.0003	−0.0000			
R(4)	77239.3265(14)	−0.0004	−0.0003	77215.9804(12)	−0.0007	−0.0012
R(5)	77239.3769(09)	0.0010	0.0006	77216.0451(12)	0.0004	−0.0006
R(6)	77239.4226(13)	0.0006	0.0005	77216.1086(19)	0.0002	−0.0005
R(7)	77239.4650(13)	−0.0003	0.0000	77216.1720(15)	−0.0001	−0.0005
R(8)	77239.5042(15)	−0.0015	0.0005	77216.2353(19)	−0.0004	0.0005
R(9)	77239.5410(12)	−0.0017	−0.0005	77216.2999(17)	0.0010	−0.0009
R(10)	77239.5751(15)	−0.0012	−0.0002	77216.3623(17)	0.0007	0.0001
R(11)	77239.6051(13)	−0.0012	0.0008	77216.4231(11)	−0.0006	−0.0007
R(12)				77216.4845(20)	−0.0002	0.0002
R(13)				77216.5431(14)	−0.0015	−0.0017
R(14)				77216.6017(16)	−0.0012	−0.0001
R(15)				77216.6590(31)	−0.0005	0.0007
R(16)				77216.7142(14)	0.0002	−0.0001
R(17)				77216.7644(22)	−0.0016	0.0008
R(18)				77216.8145(25)	−0.0008	0.0024
R(19)				77216.8561(30)	−0.0053	−0.0006
R(20)				77216.8975(43)	−0.0065	0.0009
P(1)	77238.9810(16)	0.0006	0.0000			
P(2)	77238.9143(20)	−0.0002	0.0006	77215.5477(31)	−0.0006	−0.0002
P(3)	77238.8447(12)	−0.0014	−0.0013	77215.4902(12)	0.0015	0.0011
P(4)	77238.7749(15)	−0.0004	−0.0005			
P(5)	77238.7019(15)	−0.0002	−0.0005	77215.3722(12)	0.0012	0.0004
P(6)	77238.6313(28)	0.0047	0.0049	77215.3147(19)	0.0018	0.0013
P(7)	77238.5480(10)	−0.0002	−0.0008	77215.2568(12)	0.0017	0.0005
P(8)	77238.4677(09)	0.0004	0.0003	77215.1976(12)	0.0001	−0.0009
P(9)	77238.3837(19)	0.0001	0.0005			
P(10)	77238.2932(11)	−0.0037	−0.0018	77215.0834(16)	0.0011	0.0014
P(11)	77238.2061(08)	−0.0010	0.0002	77215.0245(16)	0.0000	−0.0009
P(12)	77238.1128(11)	−0.0011	−0.0002	77214.9682(16)	0.0019	0.0003
P(14)				77214.8486(16)	0.0008	−0.0002
P(15)				77214.7899(10)	0.0029	0.0009
P(16)				77214.7259(10)	0.0010	0.0000
P(17)				77214.6623(20)	0.0012	−0.0003
P(18)				77214.5995(34)	0.0040	0.0006
P(19)				77214.5287(10)	0.0012	−0.0002
P(20)				77214.4572(16)	0.0002	−0.0010
P(21)				77214.3844(30)	0.0008	0.0005
P(22)				77214.3041(43)	−0.0027	−0.0010

combining rules to the properties of potentials for Ar_2 and Xe_2 [5,6], or on semiempirical analysis of scattering, virial and transport coefficient data using model potentials which incorporated theoretical C_6, C_8 and C_{10} long-range inverse-power dispersion energy coefficients [4,8]. Unfortunately, the absence of spectroscopic data at that time meant that the equilibrium distance and well depths of the resulting potentials had limited precision. The present work therefore sets out to determine a more accurate potential energy function by performing direct fits of analytic potential energy functions to combinations of the new VUV data presented above, the microwave data of Jäger et al. [13], and the virial coefficient data from Refs. [19–21] summarized in Table 5.

As in any least-squares fitting procedure, the objective is to minimize the dimensionless χ^2 value for the selected data set

$$\overline{\chi^2} = \sum_{i=1}^{N} \left[\frac{y_i^{calc} - y_i^{obs}}{\sigma_i} \right]^2 \tag{3}$$

with respect to variation of the parameters p_j defining the model potential energy function. For the spectroscopic data, the observed transition energies y_i^{obs} are simply the differences between the energies of the upper and lower levels involved in a particular transition i, or the energies of the ground-state levels obtained by building combination differences. For the $X\,0^+$ state, the level energies are the eigenvalues of the effective radial Schrödinger equation

$$\left[-\frac{\hbar^2}{2\mu} \frac{d^2}{dR^2} + hcV_J(R) \right] \Psi_{vJ}(R) = hcE_{vJ}\Psi_{vJ}(R), \tag{4}$$

in which the effective radial potential is the sum of the Ar–Xe interaction potential $V(R)$ and a centrifugal term which takes the effect of the molecular rotation into account

$$V_J(R) = V(R) + \frac{h}{8\pi^2\mu c} \frac{J(J+1)}{R^2}. \tag{5}$$

For any given vibration–rotation level (v,J), Eq. (4) may be solved to any required precision using standard numerical methods [27,28] to yield the associated eigenvalue E_{vJ} and eigenfunction $\Psi_{vJ}(R)$. The latter may then be used in the Hellmann–Feynman theorem expression

$$\frac{\partial E_{vJ}}{\partial p_j} = \left\langle \Psi_{vJ}(R) \left| \frac{\partial V(R)}{\partial p_j} \right| \Psi_{vJ}(R) \right\rangle \tag{6}$$

to obtain the partial derivatives required by the least-squares procedure. Similarly, the interaction virial coefficients $y_i^{obs} = B_{12}(T_i)$ may be calculated as described in Ref. [29], and the required partial derivatives determined either by taking differences, or by evaluating the integral expressions obtained on taking the partial derivatives of the expressions in Eqs. (14)–(16) of Ref. [29] with respect to the potential energy function parameters p_j.

Table 3
Experimental level energies $E_{v''J''}$ relative to the ground state, and deviations ΔE between them and values calculated from three proposed potential for the X 0^+ ground state of $^{40}Ar^{132}Xe$, all in cm^{-1}.

v''	J''	E(obs)/hc	ΔE(calc-obs)/hc		
		This work[1]	TT[2]	MLR[3]	HFD[4]
0	0	0.0000(6)[5]	−0.0000	0.0000	0.0000
0	1	0.0643(04)[5]	−0.0002	−0.0002	0.0007
0	2	0.1920(05)	0.0003	0.0004	0.0029
0	3	0.3847(04)	−0.0001	0.0001	0.0050
0	4	0.6399(05)	0.0010	0.0013	0.0096
0	5	0.9612(05)	0.0001	0.0006	0.0129
0	6	1.3436(05)	0.0021	0.0028	0.0201
0	7	1.7935(05)	0.0006	0.0015	0.0246
0	8	2.3041(05)	0.0024	0.0035	0.0332
0	9	2.8807(06)	0.0021	0.0034	0.0405
0	10	3.5213(05)	0.0016	0.0032	0.0486
0	11	4.2265(04)	0.0003	0.0023	0.0567
0	12	4.9923(05)	0.0022	0.0045	0.0689
0	13	5.8254(06)	0.0005	0.0031	0.0783
0	14	6.7199(07)	0.0009	0.0040	0.0907
0	15	7.6802(09)	0.0009	0.0026	0.1018
0	16	8.6984(11)	0.0029	0.0069	0.1193
0	17	9.7883(15)	−0.0017	0.0028	0.1293
0	18	10.9326(16)	0.0026	0.0076	0.1490
1	0	23.4445(10)[5]	0.0012	0.0005	0.5420
1	1	23.5059(07)[5]	0.0009	0.0002	0.5424
1	2	23.6292(06)	−0.0002	−0.0007	0.5427
1	3	23.8114(06)	0.0009	0.0006	0.5458
1	4	24.0554(06)	0.0013	0.0012	0.5488
1	5	24.3606(07)	0.0015	0.0017	0.5524
1	6	24.7246(06)	0.0039	0.0045	0.5589
1	7	25.1531(09)	0.0028	0.0039	0.5625
1	8	25.6418(06)	0.0024	0.0040	0.5675
1	9	26.1927(07)	0.0008	0.0029	0.5719
1	10	26.8032(06)	0.0003	0.0030	0.5781
1	11	27.4745(06)	−0.0002	0.0032	0.5850
1	12	28.2082(07)	−0.0024	0.0017	0.5908
1	13	29.0022(07)	−0.0044	0.0006	0.5976
1	14	29.8545(09)	−0.0041	0.0017	0.6073
1	15	30.7695(17)	−0.0060	0.0006	0.6154
1	16	31.7411(07)	−0.0043	0.0033	0.6278
		Average:	-0.0003_7	0.0023_8	0.3065
		RMSD about the mean:	0.0021_8	0.0018_8	0.2627

[1] From combination differences. The uncertainties correspond to the relative experimental standard deviations (the uncertainty in the absolute wave numbers is 0.015).
[2] Energies calculated from our 2-parameter Tang–Toennies-type model potential.
[3] Energies calculated from our recommended 4-parameter MLR potential.
[4] Energies calculated from the 'HFD' potential of Ref. [4].
[5] The positions of the $J''=0$ and $J''=1$ states cannot be determined from combination differences. Therefore, the calculated values are given.

Table 4
Band constants (all in cm^{-1}) for the $v''=0$ and 1 levels of the X 0^+ ground state of $^{40}Ar^{132}Xe$ and $^{40}Ar^{136}Xe$, and for the $v'=2$ level of the corresponding D 0^+ states, as determined by fitting our new VUV data and the MW data of Ref. [13] to Eqs. (1) and (2). The least-squares fits gave $\overline{dd}=1.35$ for $^{40}Ar^{132}Xe$ and 1.82 for $^{40}Ar^{136}Xe$.

Parameter	$^{40}Ar^{132}Xe$		$^{40}Ar^{136}Xe$	
	This work	Literature[1]	This work	Literature[1]
$\tilde{\nu}_{20}$	77239.103(15)[2]		77239.044(15)[2]	
$\tilde{\nu}_{21}$	77215.658(15)[2]		77215.670(15)[2]	
B'_2	0.0308756(49)		0.0306832(67)	
$D'_2/10^{-7}$	11.297(133)		10.007(215)	
B''_0	0.032065309(8)	0.03206530866(133)	0.031848135(12)	0.0318481341(27)
B''_1	0.0305978(45)		0.0303889(68)	
$D''_0/10^{-7}$	2.21706(67)	2.21705(26)	2.18525(161)	2.185078(867)
$D''_1/10^{-7}$	2.877(108)		2.042(198)	
$H''_0/10^{-12}$	−5.717[3]	−5.717(170)	−6.538[3]	−6.538(900)

[1] Values from Ref. [13].
[2] Estimated absolute uncertainty.
[3] Values taken from Ref. [13] and kept constant during the fits.

The overall quality of fit may be characterized by the dimensionless root-mean-square deviation

$$\overline{dd} = \overline{dd}(\text{tot}) = \sqrt{\chi^2/N}, \tag{7}$$

where N is the total number of data considered. However, it is often also convenient to consider the values of this quantity for subsets of the overall data set, using $\overline{dd}$(VUV), $\overline{dd}$(MW) and $\overline{dd}$(virial) for the VUV, microwave, and virial coefficient data, respectively.

Table 5
Comparison of experimental interaction virial coefficients for ArXe (B_{12}^{exp}, in units [cm^3 mol^{-1}]) with values calculated from two of the fitted potential energy functions (B_{12}^{calc}) using the mass of ^{40}Ar with the average atomic mass for Xe.

T	B_{12}^{exp}	ΔB_{12}(calc-exp)	
		2-Parameter TT	4-Parameter MLR
173.2[1]	−141.2 ±2.0	−1.67	2.11
198.2[1]	−108.0 ±2.0	−2.76	0.19
223.2[1]	−86.5 ±2.0	−1.21	1.17
273.2[1]	−56.2 ±2.0	−0.75	0.90
323.2[1]	−36.7 ±2.0	−0.76	0.45
203.0[2]	−95.0 ±6.0	−10.76	−7.94
213.0[2]	−84.5 ±6.0	−11.78	−9.19
233.0[2]	−72.8 ±6.0	−7.57	−5.37
253.0[2]	−63.0 ±6.0	−4.56	−2.67
269.0[2]	−55.5 ±6.0	−3.50	−1.80
278.0[2]	−51.8 ±6.0	−2.91	−1.31
295.0[2]	−43.5 ±6.0	−3.97	−2.53
330.0[2]	−32.9 ±6.0	−2.45	−1.29
355.0[2]	−26.2 ±6.0	−2.22	−1.22
370.0[2]	−23.2 ±6.0	−1.60	−0.67
400.0[2]	−17.5 ±6.0	−1.00	−0.21
415.0[2]	−15.0 ±6.0	−0.75	−0.03
430.0[2]	−12.7 ±6.0	−0.53	0.14
460.0[2]	−8.7 ±6.0	−0.05	0.51
500.0[2]	−4.3 ±6.0	0.54	1.00
343.0[3]	−30.5 ±6.0	−1.10	−0.02
410.0[3]	−15.6 ±6.0	−1.04	−0.30
482.0[3]	−5.1 ±6.0	−0.79	−0.28
555.0[3]	2.4 ±6.0	−0.64	−0.31
626.0[3]	4.9 ±6.0	2.33	2.53
695.0[3]	9.5 ±6.0	1.71	1.91
$\overline{dd}$(virials)		0.77	0.54

[1] Experimental values from Ref. [21].
[2] Experimental values from Ref. [19].
[3] Experimental values from Ref. [20].

4.2. A two-parameter Tang–Toennies-type model potential

This study considers two types of model potential energy functions. The first is a version of the Tang–Toennies form [5,6] which incorporates theoretical long-range coefficients and has two free parameters. In this form, the overall potential is written as a sum of a Born–Mayer-type repulsion term and an attractive term consisting of a sum of damped long-range dispersion terms

$$V(R) = Ae^{-bR} - \sum_{m=3}^{8} f_{2m}(R,b)\frac{C_{2m}}{R^{2m}}, \tag{8}$$

in which the damping functions

$$f_{2m}(R,b) = 1 - e^{bR}\sum_{k=0}^{2m}\frac{(bR)^k}{k!}, \tag{9}$$

empirically represent the effects of charge-overlap and prevent the R^{-2m} terms from dominating the interaction at short internuclear separations. This function is written in terms of the eight parameters $A, b, C_6, C_8, C_{10}, C_{12}, C_{14}$ and C_{16}. The leading long-range parameters $C_6 = 134.5E_ha_0^6$, $C_8 = 4670E_ha_0^8$ and $C_{10} = 184300E_ha_0^{10}$ were fixed at the values recommended by Tang and Toennies [6], and the recursion relation derived in Ref. [30] was then used to generate values of $C_{12} = 8499653E_ha_0^{12}$, $C_{14} = 446592027E_ha_0^{14}$ and $C_{16} = 26025079155E_ha_0^{16}$. This leaves two free parameters to be varied in the fit. Following Ref. [29], the definition of R_e as the distance at which $dV(R)/dR = 0$ allows us to express the pre-exponential factor A in terms of the other parameters,

$$A = +\frac{e^{bR_e}}{b}\left.\frac{dV_{att}(R)}{dR}\right|_{R=R_e}, \tag{10}$$

in which case the actual free parameters become R_e and b. Moreover, since

$$V(R_e) = -\mathfrak{D}_e = Ae^{-bR_e} - \frac{e^{bR_e}}{b}\left.\frac{dV_{att}(R)}{dR}\right|_{R=R_e}, \tag{11}$$

we can readily determine the value of $\mathfrak{D}_e$ associated with given values of R_e and b, as well as the associated uncertainties.

The Tang–Toennies-type potential energy function, with only two free parameters, represents an excellent compromise between providing an accurate description of the experimental data and requiring a minimal number of adjustable parameters. In particular, it reproduces the experimental data better than the two-parameter MLR model potential (see below). However, it was unable to describe the full range of experimental data within their estimated uncertainties (see Section 4.4).

4.3. A multiparameter Morse/long-range (MLR) model potential

The most accurate description of the experimental data is provided by the 'Morse/long-range' (MLR) potential of Refs. [31–33] which also incorporates the desired inverse-power-sum long-range tail, but has a more flexible multi-parameter form. The basic structure of an MLR potential energy function is [31,32]

$$V_{MLR}(R) = \mathfrak{D}_e\left[1 - \frac{u_{LR}(R)}{u_{LR}(R_e)}e^{-\beta(R)\cdot y_p^{eq}(R)}\right]^2, \tag{12}$$

in which $\mathfrak{D}_e$ is the well depth and R_e the equilibrium internuclear distance. The radial variable in the exponent is

$$y_p^{eq}(R) \equiv \frac{R^p - {R_e}^p}{R^p + {R_e}^p}, \tag{13}$$

and the exponent coefficient $\beta(R)$ is defined so that

$$\lim_{R\to\infty}\beta(R) \equiv \beta_\infty = \ln\{2\mathfrak{D}_e/u_{LR}(R_e)\}. \tag{14}$$

As a result, the function $u_{LR}(R)$ defines the long-range behavior of the potential energy function to be

$$V(R) \simeq \mathfrak{D}_e - u_{LR}(R) + \cdots, \tag{15}$$

while the denominator factor $u_{LR}(R_e)$ in Eq. (14) is simply the value of the long-range function evaluated at the equilibrium bond length. In the present case, the exponent coefficient function is written as[1]

$$\beta(R) = \beta_p^q(R) \equiv y_p^{eq}(R)\beta_\infty + \left[1 - y_p^{eq}(R)\right]\sum_{i=0}^{N}\beta_i[y_p^{eq}(R)]^i. \tag{16}$$

As in the TT-type model described above, the long-range tail of the MLR potential is defined in terms of a sum of damped dispersion terms

$$u_{LR}(R) = \sum_{m=6(2)}^{10} D_m^{mD}(R)\frac{C_m}{R^m}. \tag{17}$$

with the three dispersion coefficients C_6, C_8 and C_{10} fixed at the values recommended in Ref. [6].[2] In this case, however, the damping function is a modified version of a form introduced by Douketis et al. [34]

$$D_m^{mD} = \left(1 - e^{-\frac{b^{mD}(\rho R)}{m} - \frac{c^{mD}(\rho R)^2}{\sqrt{m}}}\right)^{m-1} \tag{18}$$

[1] Since all of the high resolution data for ArXe is directly associated with a modest range of R near the potential minimum, there is no need to utilize the $R_{ref} > R_e$ and $q < p$ extensions of the MLR model which were introduced in Ref. [32].
[2] Note that different labelling conventions are used for the summation powers in Eqs. (8) and (17).

Table 6
Results of fits to various combinations of the three types of data for ArXe. Numbers in parentheses are the uncertainties in the last digits shown, defined as 95% confidence limit uncertainties (approximately two sigma). "#free shape parameters" refers to the number of fitted β_i coefficients.

From	#Free shape parameters	Data	$\overline{dd}$(VUV)	$\overline{dd}$(MW)	$\overline{dd}$(virials)	$\overline{dd}$(total)	$\mathfrak{D}_e$/cm^{-1}	R_e/Å
UV data alone								
TT	0	130	3.06	–	–	3.06	131.3(15)	4.09577 (19)
MLR	0	130	4.41	–	–	4.41	123.27 (8)	4.0891 (44)
MLR	1	130	0.552	–	–	0.552	132.09 (26)	4.09602 (58)
MW data alone								
MLR	0	26	–	70.6	–	70.6	122.0 (11)	4.08963 (35)
MLR	1	26	–	0.343	–	0.343	132.38 (2)	4.095675 (12)
Virial data alone								
MLR	0	26	–	–	0.532	0.532	134.55 (88)	4.028 (59)
MLR	1	26	–	–	0.498	0.498	209.(38)	3.53 (20)
UV and MW data								
MLR	0	156	6.30	77.9	–	32.3	123.18 (16)	4.00052 (52)
MLR	1	156	0.582	1.26	–	0.741	132.19 (4)	4.095614 (23)
MLR	2	156	0.575	0.354	–	0.545	129.67 (52)	4.095782 (36)
UV and virial coefficient data								
TT	0	156	3.06	–	0.77	2.32	131.3 (15)	4.09577 (15)
MLR	0	156	4.41	–	2.94	4.20	123.27 (8)	4.0891 (39)
MLR	1	156	0.568	–	0.923	0.641	131.80 (27)	4.09577 (63)
MLR	2	156	0.553	–	0.533	0.550	130.01 (62)	4.09640 (57)
MW and virial coefficient data								
MLR	0	52	–	70.6	3.271	49.9	121.97 (77)	4.08963 (25)
MLR	1	52	–	0.348	1.102	0.817	132.31 (5)	4.095672 (27)
MLR	2	52	–	0.337	0.533	0.446	130.04 (43)	4.095759 (21)
All data: $\mathfrak{D}_e$ free								
MLR	0	182	6.30	77.9	2.971	29.9	123.17 (15)	4.090052 (47)
MLR	1	182	0.581	1.266	1.061	0.794	132.18 (4)	4.095611 (24)
MLR	**2**	**182**	**0.574**	**0.372**	**0.539**	**0.544**	**129.81 (38)**	**4.095773 (29)**
MLR	3	182	0.575	0.352	0.533	0.543	129.94 (49)	4.095769 (31)
All data: $\mathfrak{D}_e$ fixed at Pibel et al.[16] value								
MLR	1	182	0.894	7.36	0.756	2.898	[131.3]	4.095083 (4)
MLR	2	182	0.571	0.889	0.763	0.655	[131.3]	4.095677 (22)
MLR	3	182	0.571	0.399	0.869	0.603	[131.3]	4.095697 (23)
MLR	4	182	0.566	0.562	0.708	0.588	[131.3]	4.09544 (17)

in which $b^{mD} = 3.30$ Å^{-1} and $c^{mD} = 0.423$ Å^{-2} [33]. As discussed in Ref. [33], the conventional Tang–Toennies damping function cannot be used with the MLR form because its short-range behavior would cause the repulsive potential wall to turn over and quadratically approach zero as $r \to 0$. Following Douketis et al. [34], the range of the damping functions is set by the system-dependent parameter

$$\rho \equiv \rho_{AB} = 2\rho_A \cdot \rho_B/(\rho_A + \rho_B) \tag{19}$$

in which $\rho_A = (I_p^A/I_p^H)^{2/3}$ is defined in terms of the ratio of the ionization potential of the atom in question (I_p^A) to that of the H atom (I_p^H). For our ArXe system, $\rho_{AB} = 1.007$. Finally, as pointed out in Ref. [31], the integer p appearing in the definition of the radial variable $y_p^{eq}(R)$ of Eq. (13) must have a value larger than the difference between the largest and smallest powers of the terms contributing to Eq. (17), so in this case we set $p = 5$.

In summary, therefore, the MLR model potentials used herein are defined by fixed values of C_6, C_8 and C_{10}, together with fitted values of $\mathfrak{D}_e$, R_e and of the $(N+1)$ β_i coefficients which define the exponent polynomial of Eq. (16). For a case with only two free parameters, all of the β_i coefficients are zero, and the summation term is omitted from Eq. (16).

4.4. Results of direct potential fits

Table 6 summarizes the results obtained on fitting different potential function models to various combinations of the 130 VUV transition data of Tables 1 and 2, the 26 microwave transitions for the five zero-spin isotopomers taken from Ref. [13], and the 26 virial coefficient data from Refs. [19–21]. While the definition of a converged fit was based upon minimization of the value of $\overline{dd}$(tot), the associated $\overline{dd}$ values for the subsets of the data used in a particular analysis are also presented. If no $\overline{dd}$ value is given for a particular data type, that fit did not include that class of data.

The first three rows of Table 6 compare the results of two- and three-parameter direct potential fits to our new VUV data. They show that when the only free parameters are $\mathfrak{D}_e$ and R_e (first two rows), the resulting potential cannot account fully for the experimental data, with root-mean-square discrepancies of ~3–4 times the estimated experimental uncertainties and ~6 times what appears to be the results of an optimal fit.[3] Inclusion of one additional free parameter (β_0) in the MLR form does then yield a potential which fully accounts for these data, but as with the two-parameter MLR form, the associated well depth uncertainty is somewhat optimistic. Freeing a second MLR exponent expansion parameter (β_1) does not improve the quality of fit significantly.

The second block of Table 6 shows that when the microwave data are considered alone, they are fully accounted for by a three-parameter MLR model potential which is quite similar to that required to explain the VUV data. It may seem somewhat surprising that a fit to the MW data alone yields a well depth which is at all reasonable, since they only probe the rotational substructure of the zero-point vibrational level. This result attests to the realistic physical behavior incorporated into the potential function form and to the fact that a simultaneous analysis of very high resolution $v = 0$ rotational data for different isotopomers implicitly provides vibrational information about the potential energy well.

Rows 6 and 7 (block 3) of Table 6 then show that when considered alone, the virial coefficient data are fully explained by a two

[3] This suggests that the relative uncertainties listed in Tables 1 and 2 may be somewhat conservative.

parameter potential, but that those data are quite insensitive to its shape.

The next three blocks (line 8–17) of Table 6 show that when any two of the three types of data are considered simultaneously, a four-parameter MLR potential (defined by $\mathfrak{D}_e$, R_e, and two 'shape parameters' β_0 and β_1) is required to account fully for all of the data. The results in block 7 show that the same is true when all three types of data are considered simultaneously. Line #20 (with bold entries) corresponds to our recommended potential function model for this system, while the results in row #21 show that allowing the model to have an additional free shape parameter does not improve the fits significantly. The parameters defining our recommended model potential for ArXe are listed in Table 7, where they are compared with those defining the TT potential (with only two fitted parameters) associated with Row #11 of Table 6. It is interesting to note that within the uncertainties, the values of $\mathfrak{D}_e$ and R_e for our recommended MLR potential are the same as those yielded by the analogous four-parameter fits to any combination of two of the three types of data (see rows 10, 14 and 17 of Table 6), and with those of this two-parameter TT potential.

It is evident that the parameter uncertainties for $\mathfrak{D}_e$ yielded by the fits for many of the cases considered in Table 6 are unrealistically small. This reflects the usual problem that the parameter uncertainty yielded by a fit to a particular model does not encompass the overall physical uncertainty in the empirical determination of that quantity, since it overlooks the effect of model dependence. While it is never possible to examine this question exhaustively, the agreement of the $\mathfrak{D}_e$ value for our recommended model with those obtained from the four-parameter MLR fits for cases which omitted one or another of the three data types is reassuring. In addition, fits were performed using four- and five-parameter models in which the long-range tail $u_{LR}(R)$ in Eq. (12) was defined by only two (C_6 and C_8), or by four (C_6–C_{12}) or five (C_6–C_{14}) inverse-power terms. Since the $\mathfrak{D}_e$ values for the 'good' fits (the models including C_{14} and/or C_{12} required a third β_i parameter) lay within the range 129.70(±0.39) to 130.19(±0.62) cm^{-1}, we believe that the ±0.038 cm^{-1} uncertainty yielded by the fit to our recommended model is a realistic measure of the overall uncertainty in this quantity.

As explained in the previous section, the two-parameter Tang–Toennies potential form provides a good description of the experimental VUV data set, although not with quite the same accuracy as the three- or four-parameter MLR potentials. Fig. 4 compares these potential functions with each other and with the earlier potential function of Aziz and van Dalen [4], while the rovibrational level positions calculated from these three potentials are compared with experimental results determined from combination differences in Table 3. Fig. 4 shows that the two-parameter TT and four-parameter MLR potential energy functions are in good agreement overall, with maximal deviations of 1.5 cm^{-1} or less at internuclear distances $R \geqslant 3.75$ Å. It is particularly striking that these potential energy functions are almost exactly parallel over the range of internuclear distances relevant for the $v = 0$ and 1 levels. The slightly larger dissociation energy of the two-parameter TT function may be attributed to the number of inverse-power terms retained in Eq. (8). The nature of the TT model is such that when the position of the potential minimum is constrained (as it is by the spectroscopy), the dissociation energy increases monotonically with the number of terms included in this inverse-power sum (this is not the case for the MLR potential, see above). Thus, a TT-type model with fewer such inverse-power terms could have a well depth closer to that of the MLR functions. However, considered alone one would have no basis for deciding where to truncate this series, and the fact that $\mathfrak{D}_e$ for the MLR potential is essentially independent of the number of inverse-power terms included in Eq. (17) lends confidence in that model's value. Deviations of the earlier potential energy function of Aziz and van Dalen [4] are larger and vary over the range of internuclear distances where the wave functions of the first two vibrational levels have larger amplitudes. Fig. 4 also shows that the short-range repulsive parts of both the two-parameter TT potential and the potential of Aziz and van Dalen [4] are significantly steeper than the four-parameter MLR potential function.

The comparison of the experimental virial coefficient data from Refs. [19–21] with those calculated with our four-parameter MLR and two-parameter TT potential energy functions presented in Fig. 5 shows that both functions adequately describe the experimental results over the entire temperature range.

Table 8 compares key parameters obtained in the present analysis with existing literature values. The results of Aziz and van Dalen (column 5) represent the most recent independent determination of a full ArXe potential from experimental data. Since no spectroscopic data was available at that time, it is no surprise that their R_e and $\Delta G_{\frac{1}{2}}$ values are not quite as accurate as those yielded by the present potentials, and while they reported no parameter uncertainties, it seems reasonable to assume that within the mutual uncertainties, their $\mathfrak{D}_e$ value agrees with the present recommended value of 129.81(±0.38) cm^{-1}.

The equilibrium bond length estimated by Jäger et al. [13] (column 6 of Table 8) was obtained by extrapolating from the $v = 0$ B_0 values they determined for different isotopomers. In view of the fact that the difference between this estimate and their value of $R_0 = 4.1402$ Å (for, say, $Ar^{132}Xe$) is more than 140 times larger than the range of R_0 values for the different isotopomers, this was a remarkably good extrapolation. However, it cannot compete with the results of a potential-fit analysis.

The Tang–Toennies results in the second-last column of Table 8 were not based on any treatment of ArXe data. Rather, they were obtained by applying combining rules to the properties of two-parameter 'TT-type' potentials for Ar_2 and Xe_2 (incorporating only C_6, C_8 and C_{10} terms) which had been determined by matching with semiempirical potentials of Aziz and co-workers [35,36]. While they provide no independent information about ArXe, they provide an interesting illustration of the power of the combining rules used therein, at least for these closed-shell mixed rare gas systems.

The final column in Table 8 presents a $\mathfrak{D}_e$ value determined by adding the zero point energy of the present four-parameter MLR potential to the value of $\mathfrak{D}_0(X0^+) = 118.5(5)$ cm^{-1} determined by Pibel et al. [16] on subtracting the Xe atom excitation energy from

Table 7
Parameters defining the two-parameter Tang–Toennies potential and the recommended MLR{$p = 5, \rho_{ArXe} = 1.007$} potential for the $X0^+$ ground-state ArXe. The numbers in brackets are the uncertainties given as two standard deviations in the last digits shown.

MLR 4-parameter potential		TT 2-parameter potential	
Parameter	Value	Parameter	Value
$\mathfrak{D}_e$/cm^{-1}	129.81 (38)	$\mathfrak{D}_e$/cm^{-1}	131.3 (15)[1]
R_e/Å	4.095773 (29)	R_e/Å	4.095774 (306)
β_0	−0.117998	b/Å	3.21809262(71294)
β_1	0.09915		
C_6/(cm^{-1} Å^6)	648207[2]	C_6/(cm^{-1} Å^6)	648207[2]
C_8/(cm^{-1} Å^8)	6302462[2]	C_8/(cm^{-1} Å^8)	6302462[2]
C_{10}/(cm^{-1}Å^{10})	69649976[2]	C_{10}/(cm^{-1} Å^{10})	69649976[2]
		C_{12}/(cm^{-1} Å^{12})	899495660[2]
		C_{14}/(cm^{-1} Å^{14})	13234609416[2]
		C_{16}/(cm^{-1} Å^{16})	215970525162[2]

[1] Determined from the fitted R_e and b values and the condition $\left.\frac{dV(R)}{dR}\right|_{R=R_e} = 0$, including an estimate of the model uncertainty.
[2] Value taken from Ref. [6] and held constant during the fits.

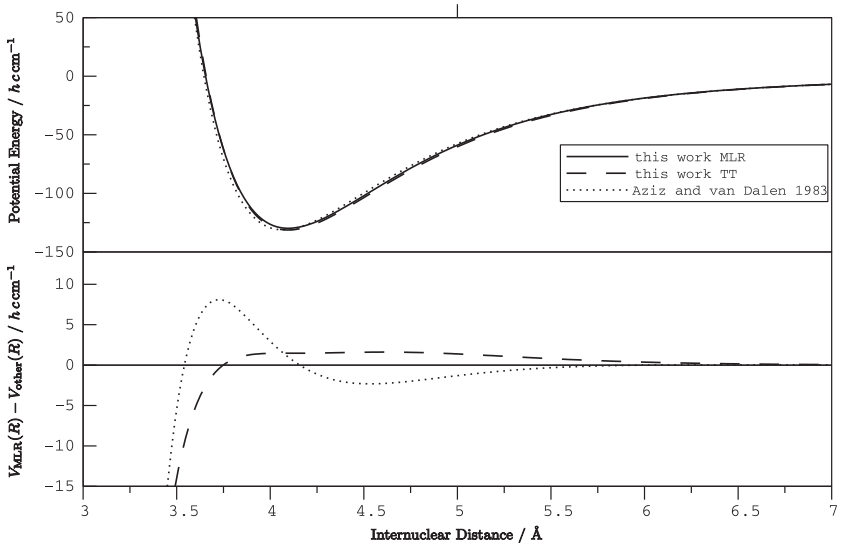

Fig. 4. Potential energy curves of the ground state of ArXe. The upper panel compares the potential curves determined in the present work (full line (MLR) and dashed line (TT)) with the potential reported in Ref. [4] (dotted line). The lower panel displays on an enlarged scale the differences between our new MLR potential curve and the other two.

the convergence limit for a series of $(v' - 0)$ bands connecting the ground-state zero-point vibrational level to vibrational levels of a shallow Rydberg state which dissociates to $Ar + Xe(6s[3/2]_1^0)$. Although this estimate only differs from our recommended $\mathfrak{D}_e = 129.81(\pm 0.38)\ cm^{-1}$ value by slightly more than the mutual uncertainties, this discrepancy is troublesome, since some of the approximations used in the analysis of the excited-state data would tend to make it give a too small, rather than too large value for $\mathfrak{D}_e$. However, the fact that the measurements of Ref. [16] lack rotational and isotopic resolution adds additional ambiguity.

As a test of this question, the last block of Table 6 presents the results of direct potential fits to our global data set in which $\mathfrak{D}_e$ was held fixed at the value determined from Ref. [16]. As is evident there, the quality of the resulting fits are significantly poorer than those for the corresponding fits in which $\mathfrak{D}_e$ was varied freely, and attempts to fit with an additional free parameter (β_4) were unsuccessful, as the 7 free parameters of the resulting model were too highly correlated to allow proper convergence to be achieved. Thus, it appears that our experimental data set is incompatible with the $\mathfrak{D}_e$ value of Ref. [16].

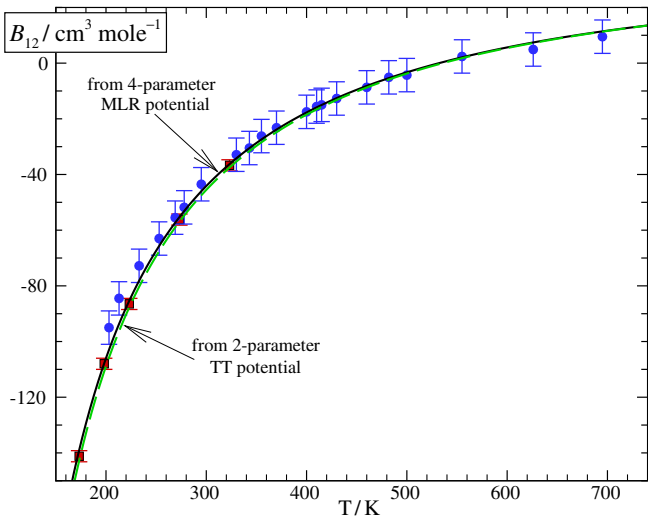

Fig. 5. Comparison of experimental virial coefficients of Schramm and co-workers [19,20] (solid round points) and of Dymond [21] (solid square points) with values calculated from our recommended MLR potential (solid curve) and from our two-parameter TT-type potential (dashed curve).

5. Conclusions

The rotationally resolved spectra of the C, D←X transitions of ArXe reported here provide new information on the rovibrational structure, on the equilibrium internuclear separation, and on the potential energy function of the $X\,0^+$ ground electronic state of ArXe. Spectra of the different isotopomers of ArXe, in particular of $^{40}Ar^{132}Xe$ and $^{40}Ar^{136}Xe$, give a consistent description of the Born–Oppenheimer ground-state potential energy function and a consistent set of spectroscopic parameters. Overall, our potential energy function is quite similar to those determined in Refs. [4,6]. However, the deviations are most significant in the bowl of the potential well and in the repulsive wall region. The potential function well depth determined herein is somewhat smaller than those reported earlier. The difference with the results of Ref. [16] is perhaps somewhat troublesome, and suggests that this system may deserve further

Table 8
Dissociation energy $\mathfrak{D}_e$, equilibrium internuclear distance R_e and lowest vibrational interval of the X 0^+ ground state of $^{40}Ar^{132}Xe$.

	Present work			Literature			
	Band constants	TT potential	MLR potential	Aziz [4]	Jäger [13]	Tang [6]	Pibel [16]
R_e/Å	–	4.095774 (153)	4.095773 (29)	4.0668	4.094(5)	4.09_1	–
$\mathfrak{D}_e$/cm^{-1}	–	131.3 (15)	129.81 (38)	131.10_5	–	130.37	131.3(5)
$\Delta G_{1/2}$/cm^{-1}	23.445	23.4457	23.4450	23.987	–	23.771	–

study, either by measuring high-resolution emission spectra from rovibrational levels of the C and D states to $v > 1$ vibrational levels of the ground state, or by repeating the experiments of Ref. [16] with higher spectroscopic and isotopic resolution.

In any case, the present analysis suggests that the four-parameter MLR potential of Table 7 is the current best potential energy function for this system. Accurate band constants $(G_v, B_v, D_v, \ldots, O_v)$ for all of the 12 bound levels of the seven main isotopomers of ArXe, and a digital listing of calculated interaction virial coefficients are included in the Supplementary Data available from the Journal's www site (see Appendix A).

Acknowledgments

This work was supported financially by the Swiss National Science Foundation under project number 200020-125030/1, and by the National Science and Engineering Research Council of Canada.

Appendix A. Supplementary data

Supplementary data associated with this article can be found, in the online version, at doi:10.1016/j.jms.2010.08.007.

References

[1] J.G. Eden, IEEE J. Sel. Top. Quantum Electron. 6 (2000) 1051–1060.
[2] J.J. Ewing, IEEE J. Sel. Top. Quantum Electron. 6 (2000) 1061–1071.
[3] R.A. Aziz, W.J. Meath, A.R. Allnatt, Chem. Phys. 78 (1983) 295–309.
[4] R.A. Aziz, A. van Dalen, J. Chem. Phys. 78 (1983) 2402–2412.
[5] K.T. Tang, J.P. Toennies, Z. Phys. D 1 (1986) 91–101.
[6] K.T. Tang, J.P. Toennies, J. Chem. Phys. 118 (2003) 4976–4983.
[7] M.V. Bobetic, J.A. Barker, J. Chem. Phys. 64 (1976) 2367–2369.
[8] R.T. Pack, J.J. Valentini, C.H. Becker, R.J. Buss, Y.T. Lee, J. Chem. Phys. 77 (1982) 5475–5483.
[9] M. Keil, L.J. Danielson, P.J. Dunlop, J. Chem. Phys. 94 (1991) 296–309.
[10] R.J. Gdanitz, J. Chem. Phys. 113 (2000) 5145–5153.
[11] R.J. Gdanitz, Chem. Phys. Lett. 348 (2001) 67–74.
[12] R.J. Gdanitz, Mol. Phys. 99 (2001) 923–930.
[13] W. Jäger, Y. Xu, M.C.L. Gerry, J. Chem. Phys. 99 (1993) 919–927.
[14] D.E. Freeman, K. Yoshino, Y. Tanaka, J. Chem. Phys. 67 (1977) 3462–3481.
[15] S.S. Dimov, X.K. Hu, D.M. Mao, J.Y. Cai, R.H. Lipson, J. Chem. Phys. 104 (1996) 1213–1224.
[16] C.D. Pibel, K. Ohde, K. Yamanouchi, J. Chem. Phys. 105 (1996) 1825–1832.
[17] S. Liu, A. Hishikawa, K. Yamanouchi, J. Chem. Phys. 108 (1998) 5330–5337. Note: In converting the values of the rotational constants from MHz as listed by Jäger et al. [13] to cm^{-1}, Liu et al. apparently approximated the speed of light to 3.0×10^{10} cm/s.
[18] O. Zehnder, F. Merkt, J. Chem. Phys. 128 (2008) 014306.
[19] B. Schramm, H. Schmiedel, R. Gehrmann, Ber. Bunsenges. 81 (1977) 316–318.
[20] H. Rentschler, B. Schramm, Ber. Bunsenges. 81 (1977) 319–321.
[21] J.H. Dymond, K.N. Marsh, R.C. Wilhoit, K.C. Wong, in: M. Frenkel, K.N. Marsh (Eds.), Landolt–Börnstein: Numerical Data and Functional Relationships in Science and Technology, New Series, Group IV: Physical Chemistry, vol. 21, Springer, 2003.
[22] U. Hollenstein, H. Palm, F. Merkt, Rev. Sci. Instr. 71 (2000) 4023–4028.
[23] Th.A. Paul, J. Liu, F. Merkt, Phys. Rev. A 79 (2009) 022505.
[24] E.R. Cohen, T. Cvitaš, J.G. Frey, B. Holmström, K. Kuchitsu, R. Marquardt, I. Mills, F. Pavese, M. Quack, J. Stohner, H.L. Strauss, M. Takami, A.J. Thor, Quantities, 3rd ed., Units and Symbols in Physical Chemistry, RSCPublishing, Cambridge, 2007.
[25] T. Tsuchizawa, K. Yamanouchi, S. Tsuchiya, J. Chem. Phys. 92 (1990) 1560–1567.
[26] L. Piticco, M. Schäfer, F. Merkt, 2010. Unpublished results.
[27] R. Meyer, J. Chem. Phys. 52 (1970) 2053–2059.
[28] R.J. Le Roy, LEVEL 7.5: A Computer Program for Solving the Radial Schrödinger Equation for Bound and Quasibound Levels, University of Waterloo Chemical Physics Research Report CP-655 (2002), See http://leroy.uwaterloo.ca/programs/.
[29] A. Wüest, F. Merkt, J. Chem. Phys. 120 (2004) 638–646.
[30] A.J. Thakkar, J. Chem. Phys. 89 (1988) 2092–2098.
[31] R.J. Le Roy, R.D.E. Henderson, Mol. Phys. 105 (2007) 663–677.
[32] R.J. Le Roy, N.S. Dattani, J.A. Coxon, A.J. Ross, P. Crozet, C. Linton, J. Chem. Phys. 131 (2009) 204309.
[33] R.J. Le Roy, C.C. Haugen, J. Tao, H. Li, Mol. Phys., in press.
[34] C. Douketis, G. Scoles, S. Marchetti, M. Zen, A.J. Thakkar, J. Chem. Phys. 76 (1982) 3057–3063.
[35] R.A. Aziz, J. Chem. Phys. 99 (1993) 4518–4525.
[36] A.K. Dham, W.J. Meath, A.R. Allnatt, R.A. Aziz, M.J. Slaman, Chem. Phys. 142 (1990) 173–189.